IEEE Access
Multidisciplinary ⋮ Rapid Review ⋮ Open Access Journal

Received November 28, 2019, accepted December 16, 2019, date of publication December 30, 2019,
date of current version January 7, 2020.

Digital Object Identifier 10.1109/ACCESS.2019.2963078

Extraction and Cross-Matching of Palm-Vein and Palmprint From the RGB and the NIR Spectrums for Identity Verification

SUNGCHUL CHO[1], BEOM-SEOK OH[2], (Member, IEEE), KAR-ANN TOH[1], (Senior Member, IEEE), AND ZHIPING LIN[3], (Senior Member, IEEE)

[1]School of Electrical and Electronic Engineering, Yonsei University, Seoul 03722, South Korea
[2]School of Digital Media Engineering, Tongmyong University, Busan 48520, South Korea
[3]School of Electrical and Electronic Engineering, Nanyang Technological University, Singapore 639798

Corresponding author: Kar-Ann Toh (katoh@yonsei.ac.kr)

This work was supported by the Basic Science Research Program through the National Research Foundation of Korea (NRF) funded by the Ministry of Education, Science and Technology under Grant NRF-2018R1D1A1A09081956.

ABSTRACT In this paper, we propose a novel cross-spectral matching system for identity verification based on the palm-vein and the palmprint acquired from the visible (RGB) and the near infrared (NIR) image spectral bands. Considering the vast availability of the visible library, the red and the blue spectrums are treated as sources of gallery samples and the NIR spectral band is utilized as the probe source without loss of generality. Apart from the extraction of palm-vein and palmprint features, the discriminative power of the palmprint templates is enhanced using a simplified Local Binary Pattern (LBP) encoding scheme. The similarity scores obtained by matching the NIR palm-vein templates against the registered RGB palm-vein templates is finally fused with scores obtained from matching the NIR palmprint codes against the registered RGB palmprint codes. Our empirical results on two publicly available multi-spectral palm databases show that the proposed system consistently achieves promising verification performance.

INDEX TERMS Cross-spectral matching, RGB, near infrared, palmprint verification, palm-vein verification, score-level fusion.

I. INTRODUCTION

Palmprint and palm-vein are two major biometric traits residing in the palm region of the hand. Due to their high stability, uniqueness and possession of rich discriminative information, both of these modalities are among the popular choices for user authentication [1]–[7]. The palmprint, which consists of the principal lines together with fine texture, can be easily acquired by the normal CCD cameras. Such ease of data acquisition has largely enabled its cost effectiveness in terms of its deployment for real-world applications [1], [2]. However, due to its utilization of information from the external skin surface, the palmprint is known to be vulnerable to forgery attacks such as faking the palmprint by a printed image. Moreover, it is sensitive to external imaging conditions such as variation of illumination [1], [2]. Worst still, a palmprint recognition system may fail when a distortion of the palmprint texture occurs during the acquisition process due to wetness and other contaminations. Under such circumstances, the palm-vein can be a good alternative for authentication since the blood vein vessels are located underneath the skin [4], [8], [9]. Moreover, utilization of the palm-vein may enhance the anti-spoof and liveness detection capability [3], [10].

Since the palmprint and the palm-vein can be complementary to each other, both the modalities can be acquired simultaneously using a specially designed system [3], [47], [48]. For example, the system in [3], [48], which consists of both the RGB and the NIR illumination sources, extracts the palmprint and the palm-vein features respectively from the RGB image and the NIR image almost at the same time. The two modalities are then fused for authentication performance enhancement. The authors of [45] proposed novel palm features based on the geometrical information of palmprint and palm-vein lines. Such a multi-sensor system has also motivated researchers to fuse palmprint features extracted

The associate editor coordinating the review of this manuscript and approving it for publication was An-An Liu.

This work is licensed under a Creative Commons Attribution 4.0 License. For more information, see http://creativecommons.org/licenses/by/4.0/

TABLE 1. Summary of existing works for palmprint and palm-vein.

		Single spectrum RGB	Single spectrum NIR	Multispectral RGB and NIR
Unimodal	Palmprint	(a) - Handcraft based: [1], [2], [5], [6], [11]–[19] - Deep learning based: [20]–[23]	(b) - Handcraft based: [24] - Deep learning based: Nil	(c) - Handcraft based: [25]–[29] - Deep learning based: [30]–[32]
Unimodal	Palm-vein	(d) - Handcraft based: [33] - Deep learning based: Nil	(e) - Handcraft based: [4], [8], [9], [34]–[39] - Deep learning based: [40]	(f) Nil
Multimodal	Palmprint + palm-vein	(g) - Handcraft based: [41], [42] - Deep learning based: Nil	(h) - Handcraft based: [10], [43]–[45] - Deep learning based: [46]	(i) Our proposed system

from multiple palmprint imaging sources under the blue (380–490*nm*), the green (490–590*nm*), the red (590–700*nm*), and the NIR (750–900*nm*) spectrums [25]. Such an approach is known as multi-spectral palmprint verification in [25].

It is noted that the above mentioned palmprint or palm-vein system each requires an additional illuminating device for amplifying either the RGB or the NIR imaging spectrum. However, utilization of an additional illuminating device may not be really necessary. Here, it is noted that extracting the palmprint from the NIR image is a viable approach because the wavelength of the visible red spectrum is very close to that of the NIR spectrum. Likewise, it is natural to think that a palm image captured under the visible red spectrum may contain not only the palmprint but also the palm-vein. This hypothesis has been verified by some recent works [33], [41], [42]. A research group in Latvia has extracted palmprint and palm-vein from respectively the blue and the red channels of the RGB image of the palm [41], [42]. Similar to the case of utilizing the RGB images, there have been a few attempts in extracting both palmprint and palm-vein from the NIR image of the palm [10], [43]–[46]. Except for [41], [45], the extracted palmprint and palm-vein features are subsequently fused for performance enhancement.

Related palmprint and palm-vein works utilizing the RGB and the NIR images are summarized in Table 1. Based on the sensing and the modality utilization, these works can be categorized as (a) RGB palmprint [1], [2], [5], [6], [11]–[23], (b) NIR palmprint [24], (c) multispectral palmprint [25]–[32], (d) RGB palm-vein [33], (e) NIR palm-vein [4], [8], [9], [34]–[40], (f) multispectral palm-vein, (g) RGB multimodal [41], [42], (h) NIR multimodal [10], [43]–[46], and (i) multispectral multimodal (our method). Each group is further divided into handcraft feature based and deep learning based methods.

Based on this table, it is observed that the existing works only explored matching of the palmprint and the palm-vein within the same sensing modality. This poses significant limitation in physical deployment. For example, the RGB image based methods [41], [42] may suffer from deteriorated imaging conditions such as variation of illumination and dryness of the palm. On the other hand, the NIR image based methods [10], [43]–[46] require both training and test samples to be acquired using the NIR imaging equipment. Thus, such NIR based methods cannot be deployed for use with the existing palm databases where the images were acquired using the RGB imaging sensors. Since groups (a) and (e) belong to the common approach and are relatively well studied, Table 2 only provides details of those less studied groups (b)-(d), (f)-(i). These two tables show that our research fills the gap of identity verification based on multiple image spectrums and multimodality of the palm.

With these motivations and observations in mind, in this paper, we propose for the first time a RGB-NIR cross-spectral matching system for palmprint and palm-vein verification. The core idea is to enable the NIR palm image (i.e., a probe image containing palmprint and palm-vein features) to be matched with those enrolled RGB palm images (i.e., the gallery images containing palmprint and palm-vein features) in the system. We propose a novel identity verification system in which both the palmprint and the palm-vein features are extracted from the RGB and the NIR palm images. Particularly, the RGB palmprint and the RGB palm-vein templates are respectively generated using images of the blue and the red spectrum while the NIR palmprint and the NIR palm-vein templates are generated using images of the NIR spectrum. Both the NIR and the RGB palmprint templates are subsequently encoded using a simplified LBP called the local directional binary code (LDBC). The proposed system is flexible in the sense that it can verify the identity using either palm-vein or palmprint only, or using both modalities via a match scores fusion.

TABLE 2. Details of groups (b)-(d), (g)-(i) in Table 1.

Author (year)	Imaging sensor (light source)	Palm-vein analysis	Palmprint analysis	Fusion of palm-vein and palmprint	**Cross-spectral matching**
(b) Extraction of palmprint from the NIR image					
Xu (2014) [24]	Public DB (NIR only)	-	NMFELM*	-	No
(c) Extraction of palmprint from the multispectral image					
Zhang (2010) [25]	Public DB (R, G, B, NIR)	-	CompCode	-	Showed correlation index of palmprint only without matching accuracy
Xu (2011) [26]	Public DB (R, G, B, NIR)	-	Not mentioned	-	Matched and fused palmprint only
Yu (2013) [27]	Public DB (R, G, B, NIR)	-	NSCT*	-	No
Bounneche (2016) [28]	Public DB (R, G, B, NIR)	-	OMLG*	-	No
Lu (2017) [29]	Public DB (R, G, B, NIR)	-	FABEMD*	-	No
Meraoumia (2017) [30]	Public DB (R, G, B, NIR)	-	PCANet*	-	No
Bensid (2018) [31]	Public DB (R, G, B, NIR)	-	DCTNet*	-	No
Zhao (2019) [32]	CMOS color (520:10:1040 nm)	-	CNN* stack	-	No
(d) Extraction of palm-vein from the RGB image					
Cho (2018) [33]	Public DB (Red and Blue)	Image processing, Gabor filtering	-	-	No
(g) Extraction of both palm-vein and palmprint from the RGB image					
Eglitis (2014) [41]	CMOS color (Red+NIR light)	Matched filter (blood vessel filter)	Matched filter (crease filter)	No	No
Nikisins (2015) [42]	CMOS color (Blue+NIR light)	HOV* on Red channel image	HOV on Blue channel image	Score level fusion	No
(h) Extraction of both the palm-vein and the palmprint from the NIR image					
Toh (2005) [43]	NIR CCD (IR light)	Image processing, vein signatures	Haar wavelet, directional energy	Score level fusion	No
Luo (2011) [44]	NIR CCD (NIR light)	DualCompCode	DualCompCode	Score level fusion	No
Li (2015) [10]	NIR CCD (NIR light)	Matched filter	CompCode	Score level fusion	No
Li (2018) [45]	NIR CCD (NIR light)	Centroid's relative radius of segments	Centroid's relative radius of segments	No	No
Zhang (2018) [46]	NIR CCD (NIR light)	Modified inception ResNet-v1	Modified inception ResNet-v1	No	No
(i) Extraction of both palm-vein and palmprint from both RGB and NIR images					
Proposed study	Public DB (R, B, NIR)	Gabor filtering, morphological	Proposed LDBC	Score level fusion	Cross-spectral matching and fusion for both palmprint and palm-vein

* Abbreviations: Nonsubsampled contour transform (NSCT), Nonnegative matrix factorization extreme learning machine (NMFELM), Oriented multiscale log-Gabor filter (OMLG), Fast and adaptive bidimensional empirical mode decomposition (FABEMD), Principal Component Analysis Network (PCANet), Discrete Cosine Transform Network (DCTNet), Convolutional Neural Network (CNN), Histogram of vectors (HOV).

The main contributions of this work are summarized as follows:

- We define for the first time a new concept of cross-spectral palm-vein and palmprint verification across the RGB and the NIR spectral bands.
- We propose a novel system in which both the palm-vein and the palmprint features are extracted from two RGB (red and blue) images and an NIR image. The proposed system can be flexibly operated using a single modality (e.g., either palm-vein or palmprint) or using both modalities via a fusion for performance enhancement.
- We propose a simplified palmprint feature encoding scheme to extract essential directional palmprint features at various scales.
- We provide extensive experiments on two public hand-palm databases comparing the proposed system with competing palmprint and palm-vein verification methods. Our results show that the proposed system outperforms the compared methods in terms of verification accuracy and computational efficiency.

This paper is organized as follows. In Section II, the essential background knowledge on a simplified Gabor filtering and the total error rate minimization classifier are presented

for immediate reference. The proposed system for palmprint and palm-vein verification across the RGB and the NIR spectral bands is introduced in Section III. In Section IV, the experimental protocols, results and discussions are provided to evident the effectiveness of the proposed system. Finally, some concluding remarks are provided in Section V.

II. PRELIMINARY

A. SIMPLIFIED GABOR FILTER

In [49], a simplified Gabor filter for face recognition has been proposed to reduce the computational load generated from the heavy convolution operation. Given the original Gabor filter as $\boldsymbol{\varphi}_{\sigma,\mu,\theta_k} \in \mathbb{R}^{w\times h}$ where σ, μ, θ_k respectively denote the standard deviation, the Gabor frequency and the orientation angle with $k \in \{1, \cdots, n\}$. Then the simplified Gabor filter is generated by quantizing the Gabor coefficients based on the following set of thresholds:

$$q_+(k_1) = \frac{A_+}{2n_p+1} \times 2k_1, \quad q_-(k_2) = \frac{A_-}{2n_n+1} \times 2k_2, \quad (1)$$

where the maximum and minimum values of the original Gabor filter coefficients are A_+ and A_-, respectively, n_p is the number of quantization level of the positive value, and n_n is the number of quantization level of the negative value. $q_+(k_1)$ at $k_1 \in \{1, 2, \cdots, n_p\}$ and $q_-(k_2)$ at $k_2 \in \{1, 2, \cdots, n_n\}$ are the positive threshold and the negative threshold, respectively (the symbols and the equations are adopted from [49]). Utilizing these thresholds, the simplified Gabor filter is generated as:

$$\boldsymbol{\varphi}^{simp}_{\sigma,\mu,\theta_k}(x,y) = \begin{cases} q_-(k_2) & (q_-(k_2) \le \boldsymbol{\varphi}_{\sigma,\mu,\theta_k}(x,y) < q_-(k_2+1)) \\ q_+(k_1) & (q_+(k_1) \le \boldsymbol{\varphi}_{\sigma,\mu,\theta_k}(x,y) < q_+(k_1+1)), \end{cases} \quad (2)$$

at pixel coordinate (x, y).

B. TOTAL ERROR RATE CLASSIFIER FOR DECISION FUSION

Apart from the popular sum-rule [50], [51], a fusion of the scores of multibiometrics can be performed based on an optimized classifier. In this work, we adopt a fast learning classifier which optimizes the desired classification error rate directly.

According to [52], the total error rate (TER) of classification is defined as the summation of the False Acceptance Rate (FAR) and the False Rejection Rate (FRR) (i.e., TER = FAR + FRR) for counting the classification error based on a decision threshold τ. Suppose m_- and m_+ are the sizes of the impostor and the genuine user respectively. Then, a classifier which is linear in its parameter vector (such as a projection model given by $g(\boldsymbol{x}) = \boldsymbol{p}(\boldsymbol{x})^T\boldsymbol{\alpha}$) can be optimized with respect to TER [52] using:

$$\boldsymbol{\alpha}_{ter} = \left[b\boldsymbol{I} + \frac{1}{m^-}\sum_{j=1}^{m^-} \boldsymbol{p}_j^T\boldsymbol{p}_j + \frac{1}{m^+}\sum_{i=1}^{m^+} \boldsymbol{p}_i^T\boldsymbol{p}_i \right]^{-1} \times \left[\frac{\tau-\eta}{m^-}\sum_{j=1}^{m^-} \boldsymbol{p}_j^T + \frac{\tau+\eta}{m^+}\sum_{i=1}^{m^+} \boldsymbol{p}_i^T \right], \quad (3)$$

where $\boldsymbol{p}_j = \boldsymbol{p}(\boldsymbol{x}_j^-) \in \mathbb{R}^d$ and $\boldsymbol{p}_i = \boldsymbol{p}(\boldsymbol{x}_i^+) \in \mathbb{R}^d$ denote the regressors respectively to the impostors and the genuine users, $\boldsymbol{x}^-$ and $\boldsymbol{x}^+$ respectively denote the feature vector of an impostor and that of a genuine user, d is the dimension of the regressor, b is a regularization parameter for stability and $\boldsymbol{I} \in \mathbb{R}^{d\times d}$ is an identity matrix. This classifier has the advantage of having an analytical solution similar to that of regression, but possesses the classification error counting capability that the regression lacks.

The category of the unseen test sample $\boldsymbol{x}_t$ is predicted using the learned $\boldsymbol{\alpha}_{ter}$ as follows:

$$g(\boldsymbol{x}_t) = \boldsymbol{p}(\boldsymbol{x}_t)^T\boldsymbol{\alpha}_{ter}, \quad (4)$$

where $\boldsymbol{p}(\boldsymbol{x}_t) \in \mathbb{R}^d$ is the test regressor generated from the test data $\boldsymbol{x}_t$. A classifier which adopts a reduced multivariate polynomial model as the regressor is called TERRM [53]

III. PROPOSED SYSTEM FOR PALM-VEIN AND PALMPRINT VERIFICATION ACROSS THE RGB AND THE NIR SPECTRUMS

In this section, we propose a cross-spectral palm biometric system for identity verification. As shown in parts (a) and (b) of Fig. 1, the core idea of the proposed system is to extract both the palm-vein and the palmprint features from *the visible gallery images* (e.g., the red spectrum image $\boldsymbol{R} \in \mathbb{R}^{p\times q}$ and the blue spectrum image $\boldsymbol{B} \in \mathbb{R}^{p\times q}$) and *the NIR probe image* $\boldsymbol{N} \in \mathbb{R}^{p\times q}$ for identity verification. As shown in part (c) of Fig. 1, the extracted RGB and NIR palmprint templates are further encoded using the proposed Local Directional Binary Code (LDBC) to strengthen the discriminant power while the obtained palm-vein templates are directly used for cross-spectral matching (see part (d) of Fig. 1). The obtained cross-spectral match scores are finally fused using the TERRM classifier [52] for performance enhancement. Each of the components mentioned above is explained in greater detail in the following subsections. Prior to the proposed processes, the input images $\boldsymbol{R}, \boldsymbol{B}$, and $\boldsymbol{N}$ are respectively normalized using the min-max normalization technique yielding $\boldsymbol{R}_{norm}, \boldsymbol{B}_{norm}$, and $\boldsymbol{N}_{norm}$.

A. PROCESSING THE RED AND THE BLUE SPECTRUMS OF PALM IMAGES

As mentioned earlier, the red spectrum palm image $\boldsymbol{R}_{norm}$ contains not only the palmprint texture but also the palm-vein vascular pattern [25] while the blue spectrum palm image $\boldsymbol{B}_{norm}$ contains almost only the palmprint texture due to its weak penetration. In this subsection, we first strengthen the palm-vein pattern in $\boldsymbol{R}_{norm}$ by suppressing the palmprint texture using $\boldsymbol{B}_{norm}$. The proposed palmprint template generation based on $\boldsymbol{B}_{norm}$ is then detailed.

1) RGB BASED PALM-VEIN TEMPLATE GENERATION

In order to keep only the palm-vein as much as possible while removing the palmprint from $\boldsymbol{R}_{norm}$, a weighted channel-wise

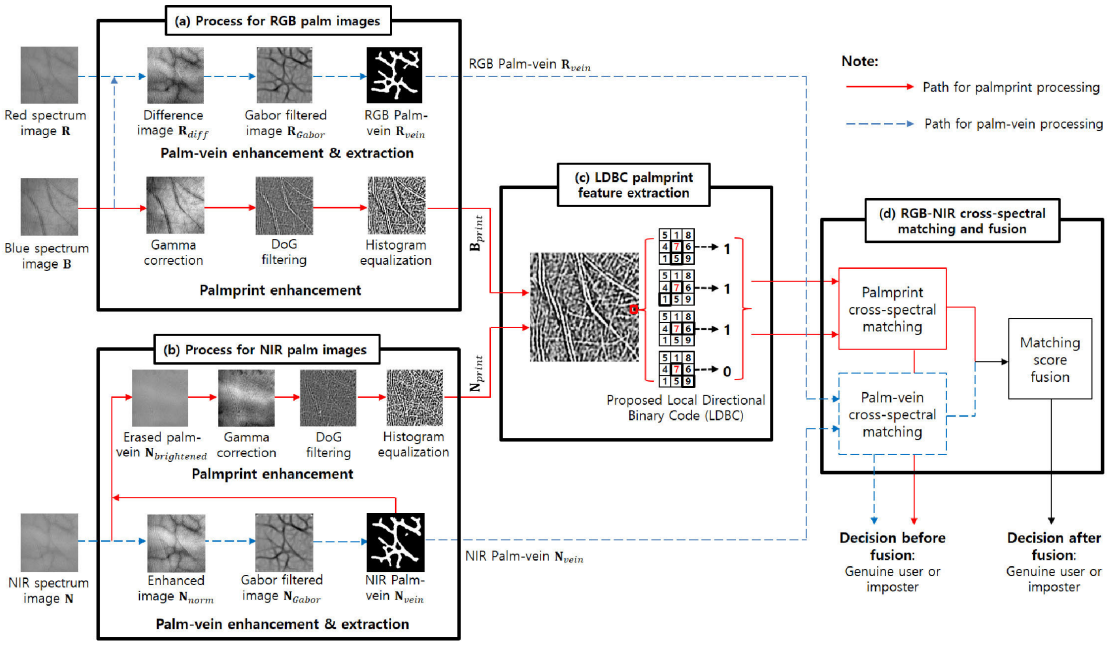

FIGURE 1. Detailed flow of the proposed system.

subtraction is proposed as follows:

$$\boldsymbol{R}_{diff} = \boldsymbol{R}_{norm} - \alpha \boldsymbol{B}_{norm}, \tag{5}$$

where $\boldsymbol{R}_{diff} \in \mathbb{R}^{p \times q}$ denotes the difference image in which the palmprint is suppressed and $0.1 \leq \alpha < 1$ is a scaling factor. Fig. 2(b) shows an example of $\boldsymbol{R}_{diff}$ obtained based on the input image of Fig. 2(a) with $\alpha = 0.5$ (see Section IV-C.1.a for details). It is observed from Fig. 2(b) that the blood vessels captured in $\boldsymbol{R}_{diff}$ appear as thick lines with smooth boundaries and with dark intensity pixels. The $\boldsymbol{R}_{diff}$ also contains some palmprint principal lines which are with thin and sharp boundaries. To keep the palm-vein lines while suppressing those unwanted principal lines, a two-step process is adopted: i) lines extraction using the simplified Gabor filtering, and ii) removal of the palmprint principal lines and noise using a morphological-like operation.

Firstly, $\boldsymbol{R}_{diff}$ is convolved with n number of kernels from the simplified Gabor function $\boldsymbol{\varphi}^{simp}_{\sigma,\mu,\theta_k}$ at $k = \{1, 2, \cdots, n\}$ generated in (2) when the real part of the original Gabor filter is adopted. The response is measured by a winner-take-all rule [11] as follows:

$$\boldsymbol{R}_{Gabor}(x, y) = \min_{k}(\boldsymbol{R}_{diff}(x, y) * \boldsymbol{\varphi}^{simp}_{\sigma,\mu,\theta_k}), \tag{6}$$

where $\boldsymbol{R}_{Gabor} \in \mathbb{R}^{p \times q}$, the symbol $*$ indicates the convolution operation. Fig. 2(c) shows the Gabor response $\boldsymbol{R}_{Gabor}$ obtained from $\boldsymbol{R}_{diff}$ of Fig. 2(b).

Prior to the morphological-like operation, the obtained Gabor response $\boldsymbol{R}_{Gabor}$ is converted into a binary map $\boldsymbol{R}_{binary} \in \mathbb{R}^{p \times q}$ as follows:

$$\boldsymbol{R}_{binary}(x, y) = \begin{cases} 1 & \text{if } \boldsymbol{R}_{Gabor}(x, y) < \overline{\boldsymbol{R}_{Gabor}}, \\ 0 & otherwise, \end{cases} \tag{7}$$

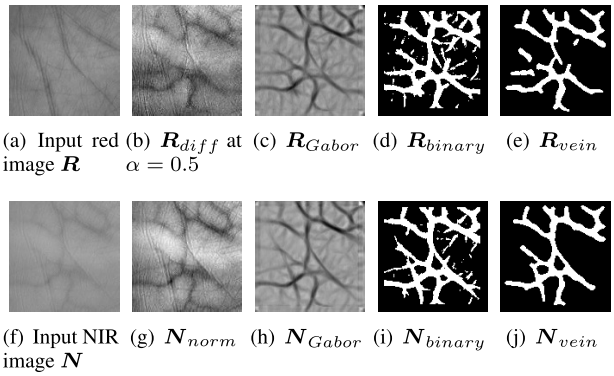

(a) Input red image $\boldsymbol{R}$ (b) $\boldsymbol{R}_{diff}$ at $\alpha = 0.5$ (c) $\boldsymbol{R}_{Gabor}$ (d) $\boldsymbol{R}_{binary}$ (e) $\boldsymbol{R}_{vein}$

(f) Input NIR image $\boldsymbol{N}$ (g) $\boldsymbol{N}_{norm}$ (h) $\boldsymbol{N}_{Gabor}$ (i) $\boldsymbol{N}_{binary}$ (j) $\boldsymbol{N}_{vein}$

FIGURE 2. Results of each processing step in palm-vein template generation obtained using a red spectrum image (see (a) to (e)) and a NIR spectrum image (see (f) to (j)).

where $\overline{\boldsymbol{R}_{Gabor}}$ indicates the pixel mean of $\boldsymbol{R}_{Gabor}$. Fig. 2(d) shows the obtained $\boldsymbol{R}_{binary}$. The proposed morphological-like operation is then implemented using a 3×3 binary mask. For each pixel, it is determined whether the pixel of interest is noise or not based on its neighborhood pixels within the mask. For example, as shown in Fig. 3, the center pixel is assigned a '1' if its neighborhood mainly consists of '1's, otherwise it is assigned a '0'. This process can be written as follows:

$$\boldsymbol{R}_{vein}(x, y) = \begin{cases} 0 & \text{if } ones_3(\boldsymbol{R}_{binary}(x, y)) = 0, \\ skip & \text{if } 0 < ones_3(\boldsymbol{R}_{binary}(x, y)) \leq \tau_{vein}, \\ 1 & \text{if } ones_3(\boldsymbol{R}_{binary}(x, y)) > \tau_{vein}, \end{cases} \tag{8}$$

where $\boldsymbol{R}_{vein} \in \mathbb{R}^{p \times q}$, $ones_3(\boldsymbol{R}_{binary}(x, y))$ returns the number of '1' elements within a 3×3 mask centered at coordinate

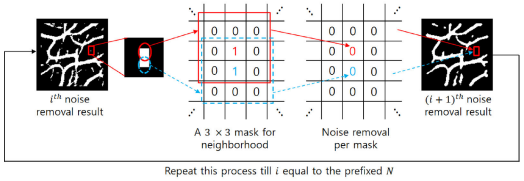

FIGURE 3. Illustration of a morphological-like process for removal of palmprint lines and noise.

(x, y), and τ_{vein} is an empirically chosen threshold to control the amount of noise removal. This process is recursively implemented until the iteration reaches a pre-defined number N. Fig. 2(e) shows the final palm-vein template $\boldsymbol{R}_{vein}$ generated using the red spectrum image $\boldsymbol{R}$ of Fig. 2(a). Although there remained minor responses from the palmprint principal lines, the obtained $\boldsymbol{R}_{vein}$ mainly consists of palm-veins.

2) RGB BASED PALMPRINT TEMPLATE GENERATION

As shown in part (a) of Fig. 1, the palmprint texture is clearly visible in the blue spectrum image $\boldsymbol{B}_{norm}$. This implies that no special process is needed to detect the palmprint texture as what we did for $\boldsymbol{R}_{diff}$ (see Section III-A.1). The key issue here is to reduce the spectral gap between the RGB and the NIR spectrums because the palmprint texture in the NIR palm images (for instance, see part (b) of Fig. 1 with palm-vein removed) is unclear in general.

To reduce the spectral gap between the RGB palmprint and the NIR palmprint, we adopt the processing sequence [54] which was utilized for face recognition, with a minor modification. The processing sequence contains a sequence of photometrical normalization techniques such as Gamma correction, difference of Gaussian (DoG), masking (optional) and equalization of variance. Its effectiveness in reducing the spectral gap has been witnessed in cross-spectral face recognition [55]. In this work, we propose to substitute the last step of equalizing the variance by equalizing the histogram. This is to strengthen the line features which is important in palmprint analysis. Part (a) of Fig. 1 shows the results of each processing step obtained on $\boldsymbol{B}_{norm}$. As shown in the part (c) of Fig. 1, the palmprint template $\boldsymbol{B}_{print}$ is subsequently encoded using the proposed LDBC (see Section III-C for detailed descriptions).

B. PROCESSING THE NIR SPECTRUM OF PALM IMAGES

Different from the images of the RGB spectrum, extracting the palmprint from the NIR spectrum is a challenging task in view of the limited amount of texture information. In this subsection, we describe the proposed generation process of the NIR palm-vein template $\boldsymbol{N}_{vein}$, which is subsequently utilized to generate the proposed NIR palmprint template $\boldsymbol{N}_{print}$.

1) NIR BASED PALM-VEIN TEMPLATE GENERATION

As shown in the part (b) of Fig. 1, a similar palm-vein template generation process for $\boldsymbol{R}_{norm}$ (see Section III-A.1) is applied to $\boldsymbol{N}$. Particularly, the $\boldsymbol{N}_{norm}$ is filtered using a set of simplified Gabor kernels in which only the minimum Gabor response is maintained (6), yielding $\boldsymbol{N}_{Gabor}$. According to (7), the obtained $\boldsymbol{N}_{Gabor}$ is next converted into a binary map $\boldsymbol{N}_{binary}$ followed by a morphological-like palmprint and noise removal as shown in (8). The final output NIR palm-vein $\boldsymbol{N}_{vein}$ is directly used for matching with the RGB palm-vein $\boldsymbol{R}_{vein}$ as shown in part (d) of Fig. 1. As a running example, Fig. 2(f)–(j) respectively show the input image $\boldsymbol{N}$ and the obtained results from each processing step.

2) NIR BASED PALMPRINT TEMPLATE GENERATION

It is observed from Fig. 2(f) that those palmprint lines appeared in $\boldsymbol{N}$ are thin and sharp. Moreover, the intensity of pixels which correspond to the palmprint lines is similar to those pixels corresponding to non-palm-vein lines. Based on these two observations, we propose to brighten the pixel intensity of those palm-vein pixels in $\boldsymbol{N}$ in order to remove the palm-vein lines.

The NIR palmprint template $\boldsymbol{N}_{print}$ generation process starts with segmenting those palm-vein pixels from $\boldsymbol{N}$ using the NIR palm-vein template $\boldsymbol{N}_{vein}$. Let $(x_i, y_i) = \{\boldsymbol{N}_{vein}(x, y) = 1\}$ where $i = 1, 2, \cdots, L$ indicates a set of pixel coordinates corresponding to the palm-vein region in $\boldsymbol{N}_{vein}$. The L number of pixels are then brightened as follows:

$$\boldsymbol{N}_{brightened}(x_i, y_i) = \boldsymbol{N}(x_i, y_i) + \frac{1}{\rho}\left(\max(\boldsymbol{\nu}) - \min(\boldsymbol{\nu})\right), \quad (9)$$

where $\boldsymbol{\nu} = \{\boldsymbol{N}(x_i, y_i)\} \in \mathbb{R}^L$ denotes a set of pixel intensities corresponding to the palm-vein region, and ρ is a scaling factor. Similar to $\boldsymbol{B}_{print}$, the modified processing sequence is applied to $\boldsymbol{N}_{brightened}$ to obtain the $\boldsymbol{N}_{print}$. The illustrative results for each step are shown in part (b) of Fig 1. This template is further encoded using the LDBC scheme as described in the following subsection.

C. LOCAL DIRECTIONAL BINARY CODE

As shown in part (c) of Fig. 1, the obtained $\boldsymbol{B}_{print}$ (see Section III-A.2) and $\boldsymbol{N}_{print}$ (see Section III-B.2) are subsequently encoded using the proposed LDBC method. The core idea of LDBC is to encode every pixel of $\boldsymbol{B}_{print}$ (and $\boldsymbol{N}_{print}$) based on its directional property of lines with respect to its neighborhood pixels in order to remove the noise. As shown in Fig. 4, the neighborhood pixels along the perpendicular direction to the line features are characterized by a significant variation of pixel intensities.

Let $\boldsymbol{P} \in \mathbb{R}^{p \times q}$ represents either $\boldsymbol{B}_{print}$ or $\boldsymbol{N}_{print}$ throughout this subsection for simplicity. Each pixel of $\boldsymbol{P}$ is encoded along four directions $\beta \in \{0, 45, 90, 135\}$ degree and at multiple scales $\gamma \in \{1, 2, \cdots, \kappa\}$ (where κ is the number of scales which is a parameter to be determined empirically by experiments) as follows (see also Fig. 5(a) for illustrative description):

$$\boldsymbol{L}_{0,\gamma}(x, y) = \begin{cases} 1 & \text{if } (\boldsymbol{P}(x, y) - \boldsymbol{P}(x, y + \gamma) \geq 0), \\ 0 & \text{otherwise} \end{cases}$$

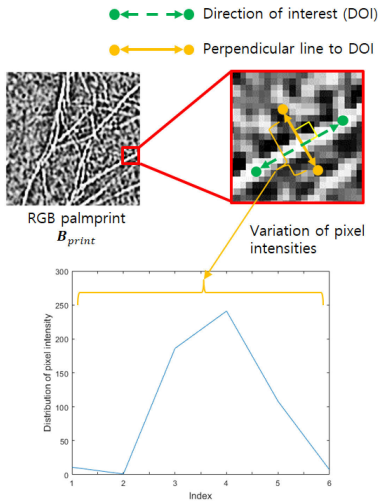

FIGURE 4. Illustrative description of the proposed LDBC feature encoding.

$$L_{45,\gamma}(x,y) = \begin{cases} 1 & \text{if } (P(x,y) - P(x-\gamma, y+\gamma) \geq 0), \\ 0 & \text{otherwise} \end{cases}$$

$$L_{90,\gamma}(x,y) = \begin{cases} 1 & \text{if } (P(x,y) - P(x+\gamma, y) \geq 0), \\ 0 & \text{otherwise} \end{cases}$$

$$L_{135,\gamma}(x,y) = \begin{cases} 1 & \text{if } (P(x,y) - P(x+\gamma, y+\gamma) \geq 0) \\ 0 & \text{otherwise} \end{cases}$$

where $L_{\beta,\gamma} \in \mathbb{R}^{(p-2\kappa)\times(q-2\kappa)}$. The 1's element at coordinate (x, y) of $L_{\beta,\gamma}$ indicates that there is a line pattern at pixel coordinate (x, y) of P captured at orientation β and scale γ. The obtained LDBC descriptors at different scales γ are finally stacked to form an overall descriptor $L_\beta \in \mathbb{R}^{(p-2\kappa)\times(q-2\kappa)\kappa}$ per direction. This encoding scheme can be considered a simplified LBP considering one effective direction. Depending on the type of input template (e.g., B_{print} or N_{print}), the obtained LDBC code L_β is denoted as L_β^{RGB} or L_β^{NIR} hereafter.

D. RGB-NIR CROSS-SPECTRAL MATCHING AND MATCH SCORES FUSION

As shown in part (d) of Fig. 1, the extracted palm-vein templates and the palmprint codes are respectively matched across the RGB and the NIR spectral bands using the Hamming distance measure. The obtained match scores from each modality are then fused using the TERRM classifier for accuracy enhancement.

Let F_i^R and F_j^N denote either the palm-vein templates (e.g., R_{vein} and N_{vein}) or the palmprint features (e.g., L_β^{RGB} and L_β^{NIR}) extracted from the i-th RGB image enrolled in the system and the j-th NIR probe image. With an aim of reducing the alignment errors occurred in the process of ROI extraction, the similarity between these two feature matrices is computed as follows [12]:

$$s_{i,j}^{\beta} = 1 - min([d_{(-\delta,-\delta)}, d_{(-\delta,-\delta+1)}, \cdots, d_{(-\delta,\delta)}, d_{(-\delta+1,-\delta)}, \cdots, d_{(\delta,\delta-1)}, d_{(\delta,\delta)}]) \quad (10)$$

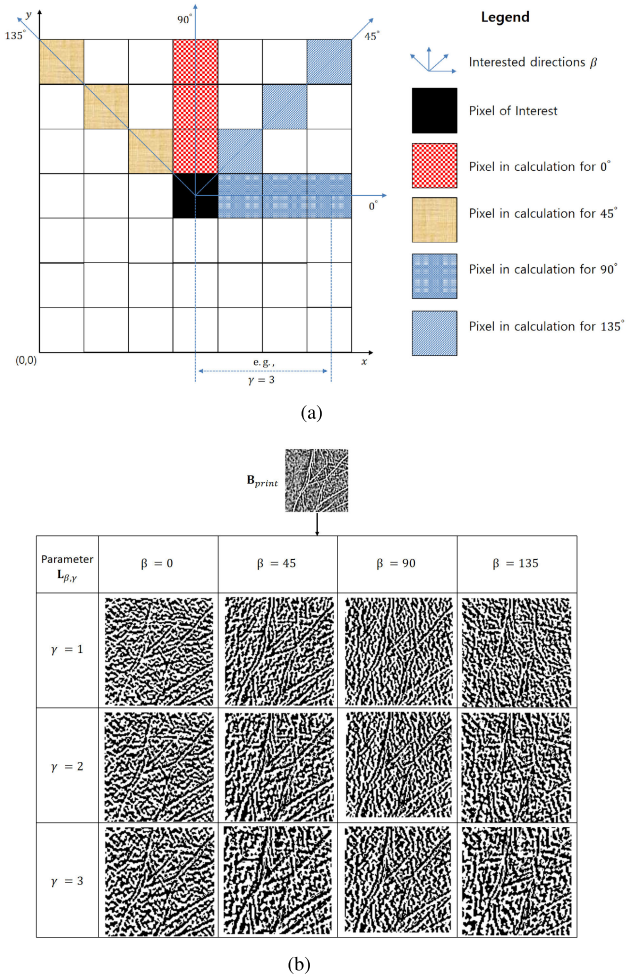

FIGURE 5. (a) Illustrative description of the proposed LDBC bit-wise encoding, and (b) examples of the LDBC descriptors obtained at $\beta \in \{0, 45, 90, 135\}$ and at $\gamma \in \{1, 2, 3\}$.

where $d_{(dx,dy)} \in \mathbb{R}$ indicates the Hamming distance between (x, y) and $(x + dx, y + dy)$ pixels given by

$$d_{(dx,dy)} = \sum_{y=1}^{p}\sum_{x=1}^{q} \frac{F_i^R(x+dx, y+dy) \oplus F_j^N(x,y)}{p \times q}, \quad (11)$$

for $dx, dy \in \{-\delta, -\delta + e, -\delta + 2e, \cdots, \delta - 2e, \delta - e, \delta\}$ with δ denoting the maximum number of pixels to be shifted, e number of bins in pixels, and $\oplus$ indicating the XOR operation. Finally, the matching score is obtained based on $s_{i,j} = \max(s_{i,j}^{\beta}), \beta \in \{0, 45, 90, 135\} = \max([s_{i,j}^{0}, s_{i,j}^{45}, s_{i,j}^{90}, s_{i,j}^{135}])$. If both F_i^R and F_j^N are from the same identity, the computed match score $s_{i,j}$ belongs to a genuine user (denoted by superscript '+'), otherwise an impostor (indicated by superscript '−').

By repeating the matching for the entire possible combinations, two sets of match scores namely, the palm-vein scores $s_v = \left[(s_v^+)^T, (s_v^-)^T\right]^T = \left[[s_{v,1}^+, s_{v,2}^+, \cdots, s_{v,m^+}^+]^T, [s_{v,1}^-, s_{v,2}^-, \cdots, s_{v,m^-}^-]^T\right]^T \in \mathbb{R}^m$, and the palmprint

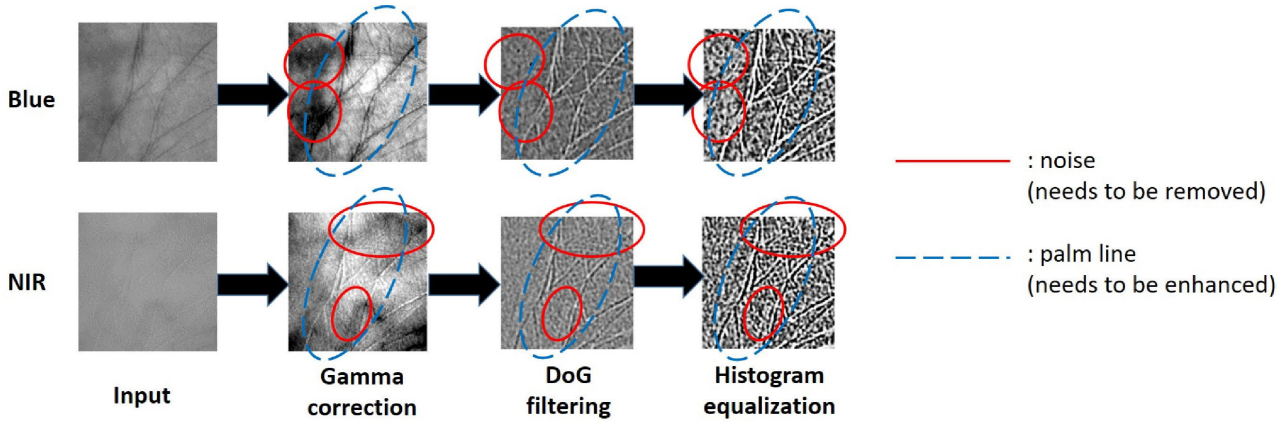

FIGURE 6. Effect of each processing step on image normalization.

scores $\boldsymbol{s}_p = \left[(\boldsymbol{s}_p^+)^T, (\boldsymbol{s}_p^-)^T\right]^T = \left[[s_{p,1}^+, s_{p,2}^+, \cdots, s_{p,m^+}^+]^T, [s_{p,1}^-, s_{p,2}^-, \cdots, s_{p,m^-}^-]^T\right]^T \in \mathbb{R}^m$ are obtained. Here, $m = m^+ + m^-$ denotes the total number of match scores for the genuine and impostor categories, $\boldsymbol{s}^+ \in \mathbb{R}^{m^+}$ and $\boldsymbol{s}^- \in \mathbb{R}^{m^-}$ respectively indicate the genuine user match scores and the impostor match scores. By stacking up these two match scores as two columns giving $\boldsymbol{S} = [\boldsymbol{s}_v, \boldsymbol{s}_p] \in \mathbb{R}^{m\times 2}$, the match scores are now treated as the m number of 2 dimensional samples. Consider a fusion classifier $g(\boldsymbol{x}) = \boldsymbol{P}_t\boldsymbol{\alpha}_{ter}$ where $\boldsymbol{\alpha}_{ter}$ is the learned TERRM model using (3) and $\boldsymbol{P}_t^T = [\boldsymbol{p}_t(\boldsymbol{x}_1), \boldsymbol{p}_t(\boldsymbol{x}_2), \cdots, \boldsymbol{p}_t(\boldsymbol{x}_m)]$ is a regressor matrix constructed using the test samples. A reduced multivariate polynomial model [56] for $\boldsymbol{p}_t$ has been adopted to transform the raw features for better discrimination.

E. ILLUSTRATIVE ANALYSIS

In this section, we provide an illustrative analysis regarding the effectiveness of adopted techniques with respect to illumination normalization, Gabor filtering, and TERRM based fusion. The following three subsections provide a detailed account regarding these techniques.

1) ILLUMINATION NORMALIZATION

The normalization techniques adopted in [54] include Gamma correction, DoG filtering, and Histogram equalization. Although these normalization techniques are used for face recognition in [54], they can also be effective for palmprint images. Fig. 6 shows the acquired images from the same palm using two different sensing spectrums from the PolyU-M database. These images show large illumination difference between the Blue and the NIR channels. After Gamma correction, the illumination gap is seen to be largely reduced. However, this also induces noise as indicated in the red solid circles. The DoG is subsequently applied to reduce the noise while retaining the palm texture. Finally, a histogram equalization is applied to enhance the image contrast. These processing steps illustrate the effectiveness of illumination gap reduction between the Blue and the NIR channels.

2) SIMPLIFIED GABOR FILTERING

Fig. 7 shows an illustrative example of an instant of image convolution using the Simplified Gabor Filters (SGF) [49] at four orientations on two images. The first image for filtering contains a dark horizontal patch and the second image contains only white pixels. At the instant of filtering the image with horizontal patch, the horizontal SGF shows the strongest filter response with low output values among the four filters. Here, we note that a group of low pixel values in an image indicates a dark image patch which shows the existence of dark palm-vein among the relatively white image. As for the second image of white pixels, a relatively weak filter response (high output value) is observed. This indicates that a convolution on a 'dark line' by a filter of 'the same direction' obtains a strong filter response. This explains how Eq. (6) can pick up oriented lines of the palm image.

3) TERRM FOR SCORE-LEVEL FUSION

Fig. 8 shows a scenario of scores distribution with decision boundaries obtained from several fusion methods namely, TER-linear, TER-RM, LSE-linear, and LSE-RM. This plot uses 100 genuine-user and 1000 impostor scores obtained from matching among the palmprint and the palm-vein images on the CASIA-M database. These decision boundaries show classification error rates of 1.49%, 1.75%, 2.31% and 3.46% respectively for TER-RM, TER-linear, LSE-RM and LSE-linear. Here, we observe that the LSE-RM method is heavily influenced by the high data density of the impostor region (i.e., fitting according to the data density). In contrast, the TER-RM method is less affected by the high impostor density because the decision boundary is determined by classification error counting. In view of this issue, the TER-RM is adopted for fusing the matching scores obtained from the palmprint and the palm-vein modalities.

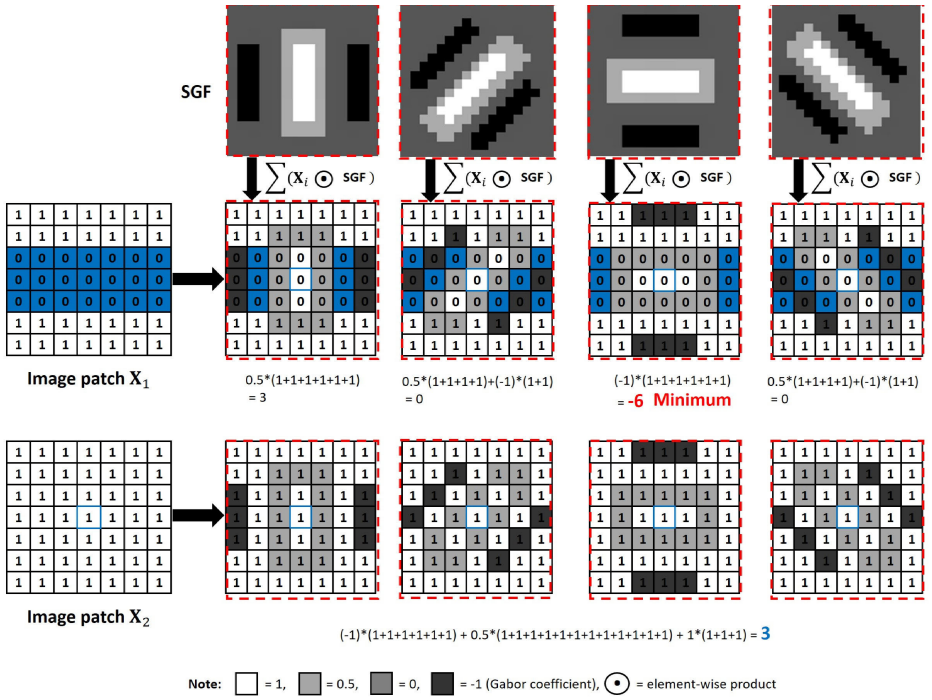

FIGURE 7. Illustrative comparison of convolution between two images using 4 different angles of Simplified Gabor Filters (SGF).

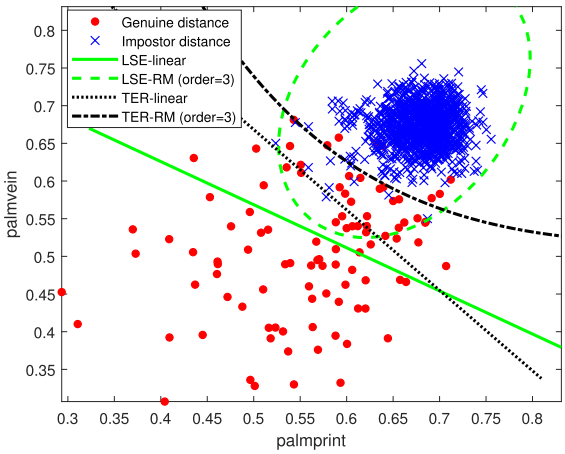

FIGURE 8. Decision boundaries of LSE-linear, LSE-RM, TER-linear and TER-RM.

IV. EXPERIMENTS

In this section, the verification performance of the proposed RGB-NIR cross-spectral matching system is evaluated via extensive empirical experiments. We first analyze the effects of each parameter of the proposed system on the verification performance. The matching capability across the RGB and the NIR spectral bands is then evaluated in terms of the Equal Error Rate (EER) and the CPU processing time. These experiments are conducted on two publicly available multi-spectral palm databases namely, the Hong Kong Polytechnic University Multispectral Palmprint database (PolyU-M) [57] and the CASIA Multi-Spectral Palmprint database (CASIA-M) [58]. The following subsections provide details of the utilized databases, the experimental settings and the obtained results together with our observations. All experiments were conducted on a PC of 3.40GHz CPU with 12 GByte RAM using Matlab [59].

A. DATABASES AND PREPROCESSING

The PolyU-M database, which consists of 24,000 images ($= 6,000 \times 4$ spectrums) from 250 subjects, is the most widely utilized database in the field of multispectral palmprint authentication. Half of the 24,000 images was taken in the first session while the remaining half was obtained in the second session. The average time interval between the two acquisition sessions was 9 days. At each session, 12 images (6 left palm and 6 right palm) were acquired from each subject using a touch-based acquisition device [25] with four different illuminations namely, the red, the green, the blue and the NIR illuminations. In other words, 48 images were taken from each subject at one session. In our performance evaluation study, excluding the images from the green illumination, 18,000 images taken under the red, the blue and the NIR illuminations are utilized.

The CASIA-M database consists of 100 subjects with 72 images per identity (7,200 images in total). These images were also acquired under 2 different acquisition sessions with 12 days of time interval. At each session, 6 images per left and right hand per subject were captured at six spectral bands (e.g., 460 nm, 630nm, 700nm, 850nm, 940nm and white light). For our experiment, a subset of 3 spectral bands namely, 460nm (blue), 700nm (red) and 850nm (NIR), from the 100 subjects are utilized. We thus have 3,600 images

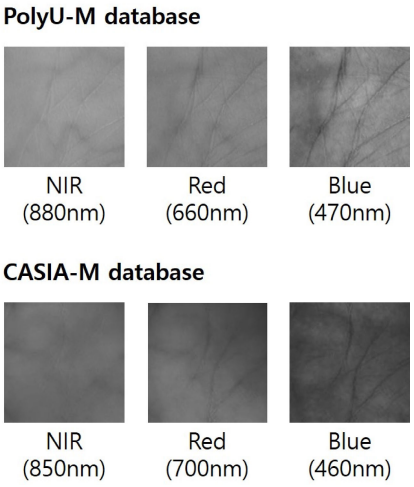

FIGURE 9. Sample images of the two databases utilized in our experimental study.

(=100 subjects × 2 sessions × 2 hands × 3 images × 3 bands) in total.

For the PolyU-M database, palm-region cropped (of 128 × 128 pixel resolution) images which are publicly available at [57] are utilized in our experiment. For CASIA-M database, the original images of 768 × 576 pixel resolution are firstly processed for ROI extraction according to [60]. Essentially, the processing steps of [60] for ROI extraction include binarization, landmark localization, and ROI cropping. Each image for preprocessing is first binarized based on a threshold process and then followed by a morphological operation for noise reduction. Subsequently, the hand contour of the binary hand image is detected using a column-wise search. Along the search, the midpoint, which lies in-between two adjacent fingers, is determined based on the middle point of the detected pair of edges. The landmark valley points are then defined based on the terminating point of the midpoint trace. Finally, the ROI is determined utilizing the detected landmark points as the reference frame [60]. Since the images of CASIA-M were acquired using a touchless sensor, they are contaminated with minor imaging noises such as distortion, translation, rotation etc. However, the images of PolyU-M are free from such noise. Several sample images of the two databases utilized in our experiments are shown in Fig. 9.

B. EXPERIMENTAL SETTINGS

1) EVALUATION PROTOCOL

The main goal of the experiments is to observe the RGB-NIR cross-spectral matching performance (e.g., accuracy and CPU processing time) of the proposed system under the identity verification scenario. Another goal is to investigate whether a fusion of the palm-vein and the palmprint helps in enhancing the identity verification accuracy of the proposed system. To achieve these two goals, as shown in Table 3, the proposed system is evaluated under three experimental settings. Under Ex-I-i), the effect of four adjustable parameters are investigated. These parameters are namely, (a) the scaling factor α which corresponds to adjusting the spectral gap between the RGB and the NIR palm-veins, (b) the scaling factor ρ which corresponds to adjusting the spectral gap between the RGB and the NIR palmprints, (c) the number of pixels δ to be shifted in feature template matching, and (d) the number of scales κ in the LDBC encoding. In Ex-I-ii) a comparison between intra- and inter-matchings has been performed.

TABLE 3. Three experiments for evaluating the proposed system.

Expt	Brief descriptions	Database
Ex-I	Empirical analysis i) for observing the parametric effect ii) comparing between intra- and inter-spectral matchings	PolyU-M
Ex-II	RGB-NIR heterogeneous identity verification under **controlled environment** (based on a contact-based sensor) i) using palm-vein only ii) using palmprint only iii) using both palm-vein and palmprint by fusion	PolyU-M
Ex-III	RGB-NIR heterogeneous identity verification under **a realistic environment** (based on a contact-free sensor) using both palm-vein and palmprint by fusion	CASIA-M

Under Ex-II and Ex-III, the main experiments with regard to the RGB-NIR cross-spectral identity verification performance of the proposed system is evaluated. In Ex-II, we evaluate the performance of the proposed system by using i) palm-vein only, ii) palmprint only, and iii) both palm-vein and palmprint via a match scores fusion. For Ex-II (i) and (ii) in which only the palm-vein templates or the palmprint templates are utilized, the test EER performances of the proposed system are compared with respective state-of-the-art NIR palm-vein (see Table 4) and RGB palmprint (see Table 5) methods including deep-learning based methods (NIR palm-vein [40], RGB palmprint [20]–[23]). Here, we note that the input images under Ex-II (ii) is given as $\boldsymbol{B}_{print}$ for the blue channel and $\boldsymbol{N}_{print}$ for the NIR channel for each competing palmprint technique. Under Ex-II (iii) and Ex-III, the EER performance and the CPU processing time of the proposed system after fusion using TERRM is compared with those obtained using state-of-the-art fusion techniques namely, the simple SUM rule [50], the support vector machine (SVM) that adopted different kernels (SVM-linear and SVM-RBF) [61], [62], and the extreme learning machine (ELM) [63].

The first half (Session 1) of the dataset (PolyU-M has 3,000 samples and CASIA-M has 1,800 samples, for each image spectrum) is used as the gallery set while the remaining half (Session 2) is used as the probe set. In Ex-I (i), the gallery set is further divided into a training set (3 samples per subject) and a validation set (3 samples per subject). This division of the gallery set is repeated 5 times using random partitioning in order to conduct 5 trials of two-fold cross-validation where the average performance is used to determine the parameter setting. Experiments Ex-I (ii), Ex-II (i)-(ii) are performed by matching between all individual samples of the visible (red and blue images) spectrum from the gallery and all individual samples of the NIR spectrum from the probe set, since there is no training process in each modality. In the fusion stage under

TABLE 4. Parametric settings of implemented competing palm-vein recognition methods.

Author	Year	Method	Parameter Settings
Zhou and Kumar [8]	2011	NMRT	$Radon_{width} = 1, Radon_{length} = 12$
		HE	$\omega_1 = 0.1^*, h_1 = 0.25^*, h_2 = 0.04^*, \tau = 3^*$
Lee [9]	2012	VeinCode	$\sigma_{vcode} = \sqrt{45}^a$, freq. = $1/11^a$, Num.orientation = 8^*
Han and Lee [34]	2012	AdaptGabor	Gabor freq. $\in \{0.07, 0.08, 0.1\}$
Wu et al. [35]	2013	MDC	$\sigma_{MDCh} = 13$, $\sigma_{MDCw} = 1$
Mirmohamadsadeghi and Drygajlo [36]	2014	LBP^b	(Num. scale, Num. sampling) = (7,16)*
		LDP	(Num. scale, Num. sampling) = (7,8), order = 3^*
Kang and Wu [4]	2014	MF-LBP^b+MPR	(Num. scale, Num. sampling) = (7,8)*, histogram bin = 256
Manmohan et al. [37]	2015	LTrP^c	(Num. scale, Num. sampling) = (9,8)
Lu et al. [38]	2016	DLBP^b	(Num. scale, Num. sampling) = (9,8), $\sigma_{DLBP} = 2.16$
Ma et al. [39]	2017	AdaptGabor2	$\sigma_{Agabor2} \in \{1, \sqrt{2}, 2\sqrt{2}, 4\}, \mu_{Agabor2} \in \{0, 0.07, 0.08, 0.1\}$
Lefkovits et al. [40]	2019	CustomCNN	SGD momentum = 0.9, batch size = 32, learning rate = 0.1
Other parameters			Num.orientation =6^{*a} [8], [35], [38] Range of grid-search = [-8:8]^a [8], [9], [34], [35], [39] Size of Gabor/Gaussian kernel = 33×33^a [9], [34], [35], [38]

- Abbreviations: Neighborhood Matching Radon Transform (NMRT), Hessian-Phase (HE), Adaptive Gabor filtering (AdaptGabor), Minimum Directional Code (MDC), Local Derivative Patterns (LDP), Mutual Forground LBP (MF-LBP), Local Tetra Pattern (LTrP), Direction of LBP (DLBP), Custom Convolutional Neural Network (CustomCNN)

*: These values are taken from the original papers

^{a}: The settings are same to our proposed method (palm-vein)

^{b}: Code source: http://www.cse.oulu.fi/CMV/Downloads/LBPMatlab

^{c}: Code source: https://github.com/rohith-ap/cbir-ltrp-matlab

Ex-II (iii) and Ex-III, the set of training scores is generated from matching between samples from the RGB Session 1 (PolyU-M: 6 samples per subject, CASIA-M: 3 samples per subject) and that of the NIR Session 1 (PolyU-M: 6 samples per subject, CASIA-M: 3 samples per subject). The set of testing match scores is obtained from matching between the visible images in the gallery set (Session 1) and the NIR images in the probe set (Session 2). The results are measured based on 5 runs of two-fold cross validation tests. For ELM, due to its random weights initialization nature, another 5 trials are performed using different random hidden weights of the ELM where the average outcomes are reported.

2) PARAMETER SETTINGS

In our method, the Gabor parameters $(\sigma, \mu, n, h, w, n_p, n_n)$ are adopted following those in [33], i.e., $\sigma = \sqrt{45}, \mu = 1/11$, $n = 6$, $h = w = 33$, $n_p = 2$ and $n_n = 1$ for Ex-I and Ex-II which utilized the PolyU-M database, and $\sigma = \sqrt{35}$ for Ex-III which utilized the CASIA-M database. The threshold τ_{vein} is empirically chosen as 4 based on the best performance of its noise removal results. The grid-search parameters are set at $e = 1$ for palm-vein and $e = 2$ for palmprint for LDBC template considering a balance between the accuracy and the computational efficiency. For the fusion algorithm TERRM, the offset and threshold parameters are set at $\tau = \eta = 0.5$ with regularization $b = 10^{-3}$ and class-specific weight (M) tuning following [52].

The four parameters in Ex-I are evaluated over $\alpha \in \{0.1, 0.2, \cdots, 1\}$ and $\rho \in \{2, 4, \cdots, 20\}$ based on the Pearson correlation [64] regarding the similarity of matching. The parameters $\delta \in \{1, 2, \cdots, 10\}$ and $\kappa \in \{1, 2, \cdots, 10\}$ are chosen based on the verification performance after fixing the values of α and ρ based on the highest correlation value. Lastly, the effect of the order of RM are observed for $r \in \{1, 2, \cdots, 6\}$. The parameter settings of compared methods under Ex-II (i) and (ii) are provided in Tables 4 and 5.

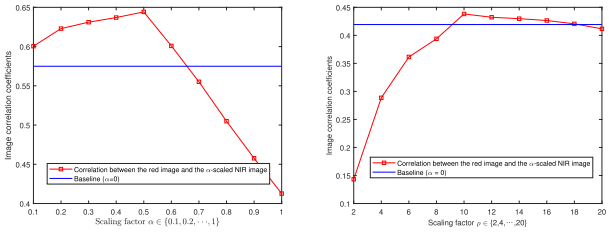

(a) Effect of α on palm-vein samples (b) Effect of ρ on palmprint samples

FIGURE 10. Effects of scaling factors α and ρ.

Due to the lack of competing methods in fusing the crossed modalities, we shall compare the performance of fusion using TERRM with that using the well-known Sum-rule, SVM and ELM. The kernel size of the RBF is searched within {[1 : 2 : 19], 50, 100}, and the number of the ELM hidden nodes is searched within {[100 : 10 : 200], 250}.

C. RESULTS AND DISCUSSION

1) (EX-I) EMPIRICAL ANALYSIS

a: EFFECTS OF SCALING FACTORS α AND ρ

Recall that, in (5), our idea to reduce the spectral gap between the RGB palm-vein and the NIR palm-vein is to subtract the red spectrum image $\boldsymbol{R}_{norm}$ by the α-scaled blue spectrum image $\boldsymbol{B}_{norm}$. Similarly, the spectral gap between the Blue palmprint and the NIR palmprint is reduced by adjusting the scaling factor ρ in (9). In Fig. 10(a), the measured correlation coefficients are plotted over the α values. As the baseline, the coefficient obtained at $\alpha = 0$ is also shown in the subplot. From this plot, the highest coefficient 0.644 is achieved at $\alpha = 0.5$. When we set $\alpha \leq 0.6$, the calculated coefficients

TABLE 5. Parametric settings of implemented competing palmprint recognition methods.

Author	Year	Method	Parameter Settings
Zhang et al. [13]	2012	E-BOCV	see common parameters
Jia et al. [14]	2014	HOL	cell size $h_c = w_c = 16^*$, block size = $32 \times 32^*$
Fei et al. [15]	2016	DOC	k = 1.6^*
Luo et al. [16]	2016	LLDP	Num.orientation =12^*
Dian and Dongmei [20]	2016	AlexNet	8 layers, activate=relu, max pooling
Minaee and Wang [21]	2017	ScatNet[b]	8×8 block, 3 layers
Li and Kim [17]	2017	LmTrP	Num. of N1 = 5, N2 = 3, N3 = 1, Num.orientation = 4^*
Sun et al. [22]	2017	CNN-F	8 layers, activate=relu, max pooling
Xu et al. [18]	2018	DRCC	$\sigma_{DRCCh} = \sigma_{DRCCw} = 1^*, h_{DRCC} = w_{DRCC} = 5^*$
Fei et al. [19]	2019	ALDC	Num. of histogram bin = 64
Genovese et al. [23]	2019	PalmNet [c]	$m_1 = m_2 = 15, k_1 = k_2 = 15, V = 15$
Other parameters			Num.orientation = 6 [13]–[15], [18], [19] Range of grid-search = [-8:2:8][a] [13]–[15], [18] Size of Gabor kernel = 9 ×9 [14], [16], [17], [19], 33 × 33 [13], [15], [18] Gabor freq. = 1/5 [14], [16], [17], [19], 1/11 [13], [15], [18] Gabor standard deviation = 5.6 [14], [16], [17], [19], $\sqrt{45}$ [13], [15], [18]

- Abbreviations: Extended Binary Orientation Co-occurrence Vector (E-BOCV), Histogram of Oriented Lines (HOL), Double-Orientation Code (DOC), Local Line Directional Pattern (LLDP), Deep scatter Network (ScatNet), Local Micro-structure Tetra Pattern (LmTrP), CNN-Fast (CNN-F), Discriminative and Robust Competitive Code (DRCC), Apparent and Latent Direction Code (ALDC), Palm Network (PalmNet)

[*]: These values are taken from the original papers

[a]: The settings are same to our proposed method (palmprint)

[b]: Code source: https://www.di.ens.fr/data/software/scatnet/download/

[c]: Code source: https://github.com/AngeloUNIMI/PalmNet

are higher than that of the baseline. However, the coefficient decreases significantly at $\alpha > 0.6$.

In Fig. 10(b), the correlation coefficient is also compared between the baseline setting and the variation with respect to ρ. As seen from this plot, the coefficients for palmprint are lower in general in which the highest coefficient of 0.438 is achieved at $\rho = 10$. This indicates that the palmprint templates $\boldsymbol{N}_{brightened}$ and $\boldsymbol{B}$ contain more noise than that of palm-vein templates. Based on these observations, we set $\alpha = 0.5$ and $\rho = 10$ in the subsequent experiments.

b: EFFECTS OF PARAMETERS δ AND κ ON THE EER AND THE CPU TIME

The impacts of δ and κ are respectively investigated in terms of the EER and CPU processing time as shown in Fig. 11. It is observed from Fig. 11(a) that the EER values decrease as the setting for both δ and κ increases. Particularly, the lowest (best) EERs are obtained at $\delta, \kappa = 10$ while the setting $\delta, \kappa = 1$ produces the worst EER performance. For δ, the results indicate that the images utilized in this empirical analysis contain alignment errors, and it can be compensated by minor image translation. The results on κ indicate that the proposed system achieves a better performance by using more LDBC features encoded at multiple scales γ (recall that $\gamma \in \{1, 2, \cdots, \kappa\}$ is one of the LDBC scale value). However, as shown in Fig. 11(b), setting higher values to both δ and κ increase not just the verification performance but also the computational cost of the proposed system. This is because a higher δ value increases the range of grid search in (10). The dimension of LDBC feature $\in \mathbb{R}^{(p-2\kappa)\times(q-2\kappa)\kappa}$ is also proportional to κ. To balance between the verification capability and the computational efficiency, we set $\delta = 8$ and $\kappa = 5$ for the subsequent experiments.

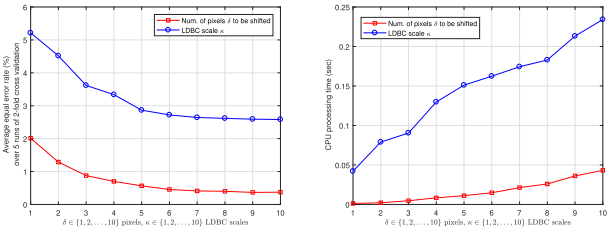

(a) EER (%) (b) CPU processing time (sec)

FIGURE 11. EER and CPU processing time performances of the proposed method with respect to the δ (□) and κ (○) parameters.

TABLE 6. EER of intra-spectral and inter-spectral matchings using the Competitive Code [11].

	intra-spectral matching			inter-spectral matching	
	Blue-Blue	Red-Red	NIR-NIR	Blue-NIR	Red-NIR
EER(%)	0.105	0.060	0.055	5.406	1.438

c: COMPARING BETWEEN INTRA-SPECTRAL AND INTER-SPECTRAL MATCHINGS

Fig. 12 shows two palm image samples of the same subject taken from the PolyU-M database. These samples show that the palm textures under the same illumination appear to be more similar than that under different illuminations. As indicated within the red solid circles in the figure, the palmprint wrinkles can be clearly seen in the Blue spectrum. These wrinkles become invisible when the illumination wavelength is longer (Blue→Red→NIR). In contrast, the palm-vein features as marked in blue dashed circles can be more clearly seen in the two samples of the NIR spectrum. These palm-veins become invisible when the spectrum wavelength is shorter (NIR→Red→Blue). This results in having a better accuracy in intra-modality

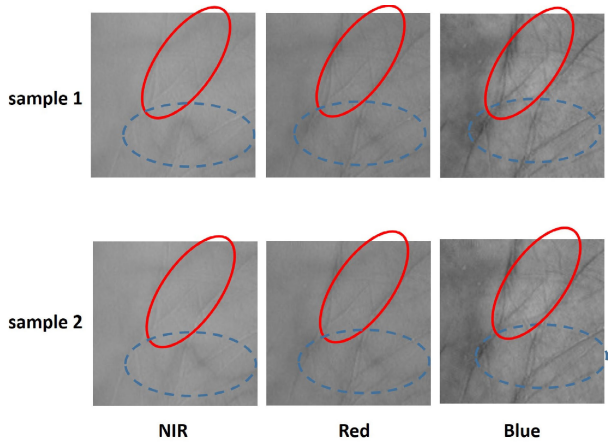

FIGURE 12. Two palm image samples of the same subject taken from the PolyU-M database.

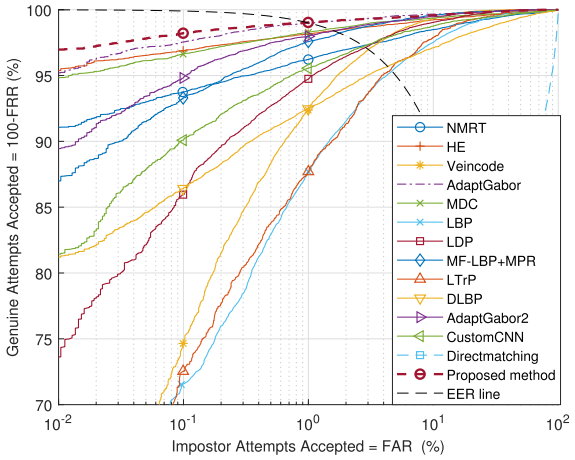

FIGURE 13. ROC curves of palm-vein methods.

TABLE 7. Test EER and FRR of the proposed system comparing with the other methods, using only palm-vein modality.

Method	year	EER (%)	FRR (%)	
			@FAR = 0.1%	@FAR = 1%
Direct matching (Red-NIR)		23.65	90.78	61.62
NMRT [8]	2011	2.74	6.25	3.78
HE [8]	2011	1.58	3.11	1.86
VeinCode [9]	2012	3.02	25.34	7.61
AdaptGabor [34]	2012	1.02	2.45	1.04
MDC [35]	2013	1.46	3.35	1.71
LBP [36]	2014	4.63	28.32	12.21
LDP [36]	2014	2.86	14.05	5.25
MF-LBP+MPR [4]	2014	1.76	6.69	2.41
LTrP [37]	2015	4.53	27.45	12.28
DLBP [38]	2016	4.31	13.55	7.49
AdaptGabor2 [39]	2017	1.62	5.18	2.01
CustomCNN [40]	2019	2.77	9.90	4.44
Proposed system (palm-vein)	2019	0.96	1.78	0.96

TABLE 8. Test EER and FRR of the proposed system comparing with the other methods, using only palmprint modality.

Method	Year	EER (%)	FRR (%)	
			@FAR = 0.1%	@FAR = 1%
Direct matching (Blue-NIR)		39.26	99.20	94.27
E-BOCV [13]	2012	5.68	29.50	13.40
HOL [14]	2014	6.18	43.98	19.19
DOC [15]	2016	3.87	10.56	6.50
LLDP [16]	2016	4.36	29.22	11.67
AlexNet [20]	2016	3.42	7.90	5.33
ScatNet [21]	2017	5.63	29.54	14.36
LmTrP [17]	2017	7.70	49.53	25.06
CNN-F [22]	2017	6.02	47.86	21.71
DRCC [18]	2018	3.86	10.90	6.16
ALDC [19]	2019	4.87	12.71	8.15
PalmNet [23]	2019	3.98	13.19	6.74
Proposed system (palmprint)	2019	3.36	11.34	5.45

matching than that in inter-modality matching. Table 6 shows the results of intra-modality and inter-modality matchings based on the well-known Competitive Code [11]. The EER values from inter-modality matching are higher than that of the intra-modality matching. Moreover, the EER value of Blue-to-NIR matching has the worst EER (5.406%) among all due to the matching across the widest spectral difference.

2) (EX-II) RGB-NIR CROSS-SPECTRAL VERIFICATION PERFORMANCE EVALUATION USING THE POLYU-M DATABASE

a: USING PALM-VEIN ONLY

Table 7 and Fig. 13 show respectively the test EER performances and the ROC curves of all compared palm-vein methods listed in Table 4. As shown in Table 7, our proposed method shows the lowest EER (best) among the compared state-of-the-arts. Among these state-of-the-arts, the ordinary LBP algorithm obtained the highest (worst) EER of 4.65% and the the AdaptGabor algorithm recorded the lowest (best) EER of 1.02%. The CustomCNN records a comparable EER of 2.77%. In terms of the ROC plots as shown in Fig. 13, our proposed method shows good matching accuracy over a wide operating range with the AdaptGabor method showing competing overall performance to our method. For example, the FRR values at FAR=0.1% and at FAR=1% in Table 7 show our proposed method gives the highest accuracy among the compared methods (i.e., FRR = 1.78% and 0.97% respectively at FAR = 0.1% and FAR=1%). These results show the effectiveness of our image processing and feature extraction design.

b: USING PALMPRINT ONLY

Table 8 and Fig. 14 show respectively the test EER performances and the ROC curves of all compared methods listed in Table 5 for palmprint verification. From Table 8, our proposed method shows the best EER of 3.36% comparing with those experimented state-of-the-art methods (see Table 8). These results in Table 8 indicate that the DOC, AlexNet, DRCC, and PalmNet methods have comparable performance with EER lower than 4%. In contrast, the HOL and the LmTrP show among the highest EERs of 6.18% and 7.70% respectively. From the overall ROC perspective as shown in Fig. 14, AlexNet shows the best verification accuracy when the FAR value is less than 1%. The proposed method maintains a relatively good performance over the entire range of the FAR values. These results illustrate the effectiveness of our encoding scheme for palmprint verification.

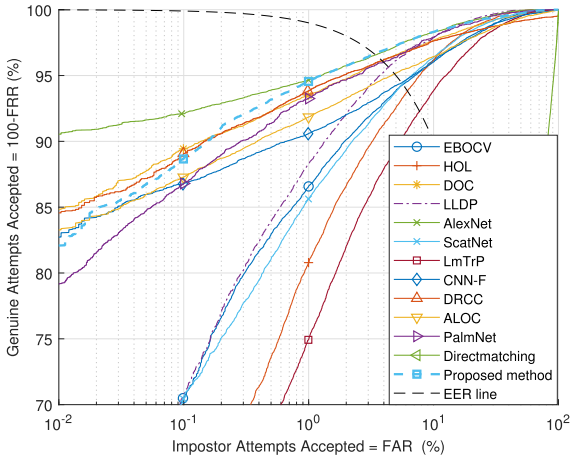

FIGURE 14. ROC curves of palmprint methods.

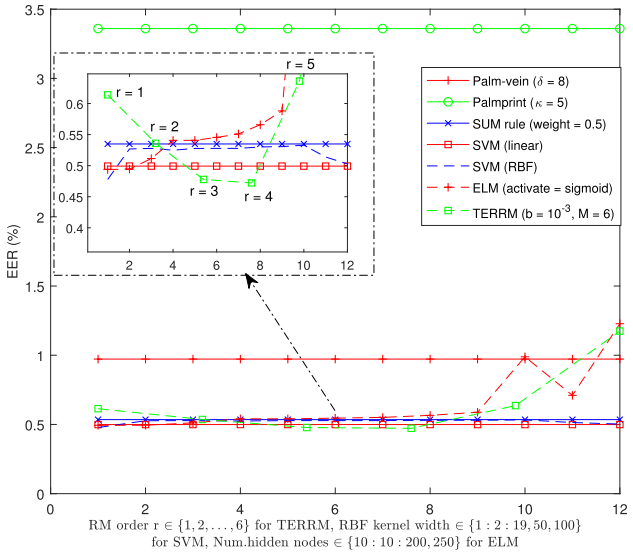

FIGURE 15. EER performance before and after fusion using the PolyU-M database.

c: UTILIZING BOTH PALM-VEIN AND PALMPRINT

Fig. 15 shows the EER values before and after fusion adopting several fusion techniques. The match-scores fusion is adopted here due to its good performance reported in [50]. Since fusion by the simple sum-rule and the SVM with linear kernel have no adjustable parameters, their results are plotted as a constant line for ease of visual comparison. Comparing with the EER performance when using only palmprint and only palm-vein, the results after fusion generally produce much better EER performance except for the case of TERRM at order $r = 6$, and the case of ELM with 250 hidden nodes (see Fig. 15). This indicates that a score fusion can generally improve the performance. Among the fusion methods, the best EERs go to TERRM at $r = 3$ (EER = 0.477%) and at $r = 4$ (EER = 0.472%). The SVM method (SVM-linear and SVM-RBF) shows comparable EER results for some of the settings. Based on the setting that gives the best EER for each method, the ROC curves and the FRR

TABLE 9. EER and FRR values on the PolyU-M database after fusion.

Method	Best EER (%)	FRR (%)	
		@FAR = 0.1%	@FAR = 1%
SVM (linear)	0.50	0.82	0.45
SVM (RBF kernel width = 1)	0.48	1.43	0.71
ELM (hidden node = 10)	0.49	1.53	0.76
TERRM (r=4)	0.47	0.76	0.39

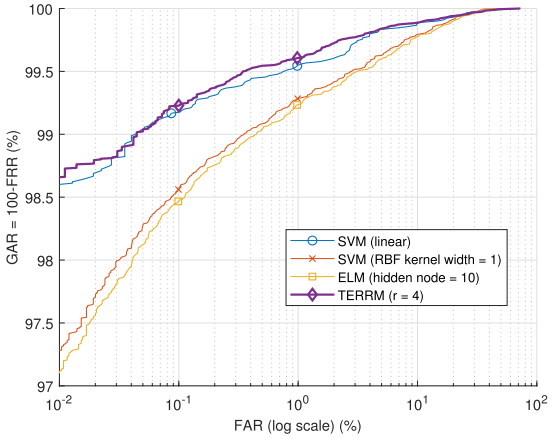

FIGURE 16. ROC curves of compared fusion methods on the PolyU-M database.

values at specific operating points are recorded. The results are shown in Fig. 16 and Table 9 where our proposed method shows good matching accuracy over a wide operating range including the points at FAR=0.1% and FAR=1% where the FRR values are 0.76% and 0.39% respectively. In terms of the computational CPU processing times, Table 10 and Fig. 17 show a different aspect of the performance. Due to the heavy search involved in seeking the supporting vectors, the SVM-RBF shows a significantly high computational cost relative to that of TERRM and the ELM. Particularly, the SVM-RBF can have as much as about 633 times slower speed than that of TERRM. The ELM, though with comparable computational cost with that of TERRM, comes with a relatively poor EER performance comparing among the fusion techniques. This result indicates that TERRM is an efficient method for fusion counting both accuracy and computational complexity.

3) (EX-III) RGB-NIR CROSS-SPECTRAL VERIFICATION PERFORMANCE EVALUATION USING THE CASIA-M DATABASE

Fig. 18 shows the EER performance before and after fusion for the CASIA-M database. Similar to the result based on the PolyU-M database, the EER after fusion shows much more improvement than that before fusion for every parameters. These results verify again, the effectiveness of fusion. Among the fusion results, the best EER is recorded for TERRM at $r = 3$ (EER = 4.277%). The SVM (SVM-RBF, SVM-linear) records good EER performance for the entire range of parameters similar to that in EX-II(iii). Similar to Fig. 16 and Table 9, the results of these fusion methods are compared based on each fixed parameter. The results in Fig. 19 and Table 11 show that the FRR value for TERRM recorded the

TABLE 10. Recorded CPU time (sec) on the PolyU-M database.

	Feature extraction (for one image)		Feature matching (for one matching pair)		For the entire set of genuine-users/impostors	Fusion times (Train / Test is per 100samples)
	Palm-vein	Palmprint	Palm-vein	Palmprint		
SVM-linear	0.094	0.104	0.043	0.128	57530.145	3.560 / 0.006
SVM-RBF						90.539 / 0.117
ELM						0.405 / 0.009
TERRM						0.143 / 0.004

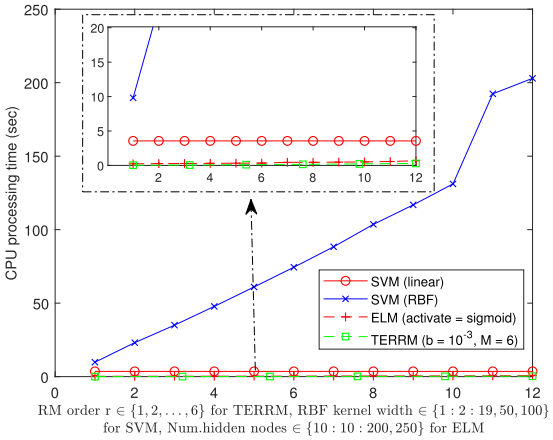

FIGURE 17. CPU training time measured using the PolyU-M database.

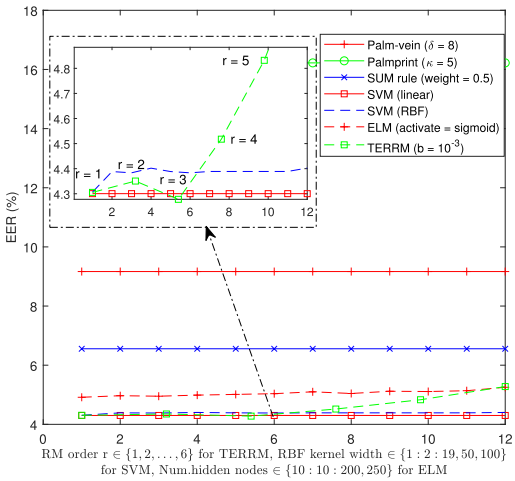

FIGURE 18. EER performance before and after fusion using the CASIA-M database.

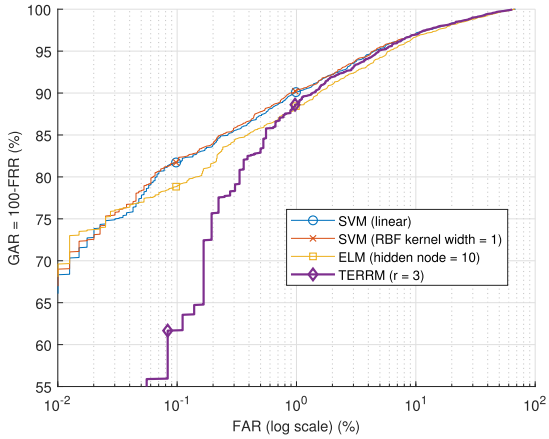

FIGURE 19. ROC curves of compared fusion methods on the CASIA-M database.

TABLE 11. EER and FRR values on the CASIA-M database after fusion.

Method	Best EER (%)	FRR (%)	
		@FAR = 0.1%	@FAR = 1%
SVM (linear)	4.30	18.25	9.86
SVM (RBF kernel width = 1)	4.31	18.25	9.75
ELM (hidden node = 10)	4.92	21.14	11.53
TERRM (r=3)	4.28	38.31	11.36

worst performance at FAR=0.1%. However, the accuracy of TERRM becomes comparable with the compared fusion methods when FAR=1%. The results for this data set show lower accuracy (higher EER) than those in Ex-II. This is reasonable because the CASIA-M database was collected using a contact-free sensor and the PolyU-M database was collected using a contact-based sensor.

4) SUMMARY OF RESULTS AND OBSERVATIONS

- The results (Fig. 10 and Fig. 11) of parametric search based on the training validation set have been utilized for parameter selection for subsequent use.
- The results of palm-vein only matching (Fig. 13) show superiority of the proposed method over the compared methods in terms of the test EER performance.
- The results of palmprint only matching (Fig. 14) show superiority of the proposed method over the compared methods in terms of the test EER performance.
- For both the PolyU-M and the CASIA-M datasets, the results of fusion (Fig. 15 and Fig. 18) show significant EER enhancement over the individual modalities.

V. CONCLUSION

A novel cross-spectral matching system has been proposed for identity verification based on the RGB and NIR images of the palm-vein and the palmprint. The main novelty of this system comes from the lack of any existing work in the literature that extracts both the palm-vein and the palmprint from each of the RGB and the NIR spectrums under a single system. This gives rise to the availability of four sets of cross-spectral feature templates for identity matching. Apart from the features extracted from both the visible and the NIR modalities, a encoding scheme based on a simplified LBP scheme has been proposed for the palmprint. The two sets of extracted features for each modality were eventually fused

at the score level for verification performance enhancement. Our experimental results under both the constrained and the unconstrained image acquisition environments showed competency of the proposed system in terms of verification accuracy as well as computational efficiency.

REFERENCES

[1] A. Kong, D. Zhang, and M. Kamel, "A survey of palmprint recognition," *Pattern Recognit.*, vol. 42, no. 7, pp. 1408–1418, Jul. 2009.

[2] D. Zhang, W. Zuo, and F. Yue, "A comparative study of palmprint recognition algorithms," *ACM Comput. Surv.*, vol. 44, no. 1, pp. 1–37, Jan. 2012.

[3] D. Zhang, Z. Guo, G. Lu, L. Zhang, Y. Liu, and W. Zuo, "Online joint palmprint and palmvein verification," *Expert Syst. Appl.*, vol. 38, no. 3, pp. 2621–2631, Mar. 2011.

[4] W. Kang and Q. Wu, "Contactless palm vein recognition using a mutual foreground–based local binary pattern," *IEEE Trans. Inf. Forensics Security*, vol. 9, no. 11, pp. 1974–1985, Nov. 2014.

[5] L. Leng and A. B. J. Teoh, "Alignment-free row-co-occurrence cancelable palmprint Fuzzy Vault," *Pattern Recognit.*, vol. 48, no. 7, pp. 2290–2303, Jul. 2015.

[6] Q. Zheng, A. Kumar, and G. Pan, "Suspecting less and doing better: New insights on palmprint identification for faster and more accurate matching," *IEEE Trans. Inf. Forensics Security*, vol. 11, no. 3, pp. 633–641, Mar. 2016.

[7] A. Kumar, "Toward more accurate matching of contactless palmprint images under less constrained environments," *IEEE Trans. Inf. Forensics Security*, vol. 14, no. 1, pp. 34–47, Jan. 2019.

[8] Y. Zhou and A. Kumar, "Human identification using palm–vein images," *IEEE Trans. Inf. Forensics Security*, vol. 6, no. 4, pp. 1259–1274, Dec. 2011.

[9] J.-C. Lee, "A novel biometric system based on palm vein image," *Pattern Recognit. Lett.*, vol. 33, no. 12, pp. 1520–1528, Sep. 2012.

[10] Q. Li, X. Li, Z. Guo, and J. You, "Online personal verification by palmvein image through palmprint-like and palmvein information," *Neurocomputing*, vol. 147, pp. 364–371, Jan. 2015.

[11] A.-K. Kong and D. Zhang, "Competitive coding scheme for palmprint verification," in *Proc. 17th Int. Conf. Pattern Recognit. (ICPR)*, Cambridge, U.K., vol. 1, Aug. 2004, pp. 520–523.

[12] W. Jia, D.-S. Huang, and D. Zhang, "Palmprint verification based on robust line orientation code," *Pattern Recognit.*, vol. 41, no. 5, pp. 1504–1513, May 2008.

[13] L. Zhang, H. Li, and J. Niu, "Fragile bits in palmprint recognition," *IEEE Signal Process. Lett.*, vol. 19, no. 10, pp. 663–666, Oct. 2012.

[14] W. Jia, R.-X. Hu, Y.-K. Lei, Y. Zhao, and J. Gui, "Histogram of oriented lines for palmprint recognition," *IEEE Trans. Syst., Man, Cybern., Syst.*, vol. 44, no. 3, pp. 385–395, Mar. 2014.

[15] L. Fei, Y. Xu, W. Tang, and D. Zhang, "Double-orientation code and nonlinear matching scheme for palmprint recognition," *Pattern Recognit.*, vol. 49, pp. 89–101, Jan. 2016.

[16] Y.-T. Luo, L.-Y. Zhao, B. Zhang, W. Jia, F. Xue, J.-T. Lu, Y.-H. Zhu, and B.-Q. Xu, "Local line directional pattern for palmprint recognition," *Pattern Recognit.*, vol. 50, pp. 26–44, Feb. 2016.

[17] G. Li and J. Kim, "Palmprint recognition with local micro-structure tetra pattern," *Pattern Recognit.*, vol. 61, pp. 29–46, Jan. 2017.

[18] Y. Xu, L. Fei, J. Wen, and D. Zhang, "Discriminative and robust competitive code for palmprint recognition," *IEEE Trans. Syst., Man, Cybern., Syst.*, vol. 48, no. 2, pp. 232–241, Feb. 2018.

[19] L. Fei, B. Zhang, W. Zhang, and S. Teng, "Local apparent and latent direction extraction for palmprint recognition," *Inf. Sci.*, vol. 473, pp. 59–72, Jan. 2019.

[20] L. Dian and S. Dongmei, "Contactless palmprint recognition based on convolutional neural network," in *Proc. IEEE 13th Int. Conf. Signal Process. (ICSP)*, Nov. 2016, pp. 1363–1367.

[21] S. Minaee and Y. Wang, "Palmprint recognition using deep scattering network," in *Proc. IEEE Int. Symp. Circuits Syst. (ISCAS)*, May 2017, pp. 1–4.

[22] Q. Sun, J. Zhang, A. Yang, and Q. Zhang, "Palmprint recognition with deep convolutional features," in *Proc. Chin. Conf. Image Graph. Technol.* Singapore, 2017, pp. 12–19.

[23] A. Genovese, V. Piuri, K. N. Plataniotis, and F. Scotti, "PalmNet: Gabor–PCA convolutional networks for touchless palmprint recognition," *IEEE Trans. Inf. Forensics Security*, vol. 14, no. 12, pp. 3160–3174, Dec. 2019.

[24] X. Xu, X. Zhang, L. Lu, W. Deng, and K. Zuo, "Fast near-infrared palmprint recognition using nonnegative matrix factorization extreme learning machine," *Optica Appl.*, vol. 44, no. 2, pp. 285–298, 2014.

[25] D. Zhang, Z. Guo, G. Lu, L. Zhang, and W. Zuo, "An online system of multispectral palmprint verification," *IEEE Trans. Instrum. Meas.*, vol. 59, no. 2, pp. 480–490, Feb. 2010.

[26] Y. Xu, Q. Zhu, and D. Zhang, "Combine crossing matching scores with conventional matching scores for bimodal biometrics and face and palmprint recognition experiments," *Neurocomputing*, vol. 74, no. 18, pp. 3946–3952, Nov. 2011.

[27] Y. Yu, Y. Tang, J. Cao, and J. Gan, "Multispectral palmprint recognition using score-level fusion," in *Proc. IEEE Internet Things, IEEE Int. Conf. IEEE Cyber, Phys. Social Comput. Green Comput. Commun.*, Beijing, China: IEEE Press, Aug. 2013, pp. 1450–1453.

[28] M. D. Bounneche, L. Boubchir, A. Bouridane, B. Nekhoul, and A. Ali-Chérif, "Multi-spectral palmprint recognition based on oriented multiscale log-Gabor filters," *Neurocomputing*, vol. 205, pp. 274–286, Sep. 2016.

[29] L. Lu, X. Zhang, X. Xu, and D. Shang, "Multispectral image fusion for illumination-invariant palmprint recognition," *PLoS ONE*, vol. 12, no. 5, May 2017, Art. no. e0178432.

[30] A. Meraoumia, F. Kadri, H. Bendjenna, S. Chitroub, and A. Bouridane, "Improving biometric identification performance using PCANet deep learning and multispectral palmprint," in *Biometric Security Privacy*. Cham, Switzerland: Springer, 2017, pp. 51–69.

[31] K. Bensid, D. Samai, F. Z. Laallam, and A. Meraoumia, "Deep learning feature extraction for multispectral palmprint identification," *J. Electron. Imag.*, vol. 27, no. 3, May 2018, Art. no. 033018.

[32] S. Zhao, B. Zhang, and C. P. Chen, "Joint deep convolutional feature representation for hyperspectral palmprint recognition," *Inf. Sci.*, vol. 489, pp. 167–181, Jul. 2019.

[33] S. Cho and K.-A. Toh, "Palm–vein recognition using RGB images," in *Proc. 3rd Int. Conf. Biomed. Signal Image Process. (ICBIP)*, Seoul, South Korea, 2018, pp. 47–52.

[34] W.-Y. Han and J.-C. Lee, "Palm vein recognition using adaptive Gabor filter," *Expert Syst. Appl.*, vol. 39, no. 18, pp. 13225–13234, Dec. 2012.

[35] K.-S. Wu, J.-C. Lee, T.-M. Lo, K.-C. Chang, and C.-P. Chang, "A secure palm vein recognition system," *J. Syst. Softw.*, vol. 86, no. 11, pp. 2870–2876, Nov. 2013.

[36] L. Mirmohamadsadeghi and A. Drygajlo, "Palm vein recognition with local texture patterns," *IET Biometrics*, vol. 3, no. 4, pp. 198–206, Dec. 2014.

[37] M. Mohan, J. Saxena, K. Teckchandani, P. Pandey, M. K. Dutta, C. M. Travieso, and J. B. Alonso-Hernandez, "Palm vein recognition using local tetra patterns," in *Proc. Int. Work Conf. Bioinspired Intell.*, San Sebastian, Spain, Jun. 2015, pp. 151–156.

[38] W. Lu, M. Li, and L. Zhang, "Palm vein recognition using directional features derived from local binary patterns," *Int. J. Signal Process., Image Process. Pattern Recognit.*, vol. 9, no. 5, pp. 87–98, May 2016.

[39] X. Ma, X. Jing, H. Huang, Y. Cui, and J. Mu, "Palm vein recognition scheme based on an adaptive Gabor filter," *IET Biometrics*, vol. 6, no. 5, pp. 325–333, 2017.

[40] L. Szidonia, L. Laszlo, and S. Szilagyi, "Applications of different CNN architectures for palm vein identification," in *Modeling Decisions for Artificial Intelligence*, vol. 11676. Cham, Switzerland: Springer, 2019, pp. 295–306.

[41] T. Eglitis, M. Pudzs, and M. Greitans, "Bimodal palm biometric feature extraction using a single RGB image," in *Proc. Int. Conf. Biometrics Special Interest Group*, Darmstadt, Germany, Sep. 2014, pp. 1–7.

[42] O. Nikisins, T. Eglitis, M. Pudzs, and M. Greitans, "Algorithms for a novel touchless bimodal palm biometric system," in *Proc. Int. Conf. Biometrics (ICB)*, Phuket, Thailand, May 2015, pp. 436–443.

[43] K.-A. Toh, H.-L. Eng, Y.-S. Choo, Y.-L. Cha, W.-Y. Yau, and K.-S. Low, "Identity verification through palm vein and crease texture," in *Advances in Biometrics*, vol. 3832. Berlin, Germany: Springer, 2006, pp. 546–553.

[44] N. Luo, Z. Guo, G. Wu, and C. Song, "Joint palmprint and palmvein verification by dual competitive coding," in *Proc. Int. Conf. Adv. Comput. Control*. Harbin, China: IEEE Press, Jan. 2011, pp. 538–542.

[45] W. Li and W.-Q. Yuan, "Multiple palm features extraction method based on vein and palmprint," *J. Ambient Intell. Humanized Comput.*, pp. 1–15, Feb. 2018, doi: 10.1007/s12652-018-0699-1.

[46] L. Zhang, Z. Cheng, Y. Shen, and D. Wang, "Palmprint and palmvein recognition based on DCNN and a new large–scale contactless palmvein dataset," *Symmetry*, vol. 10, no. 4, p. 78, Mar. 2018.

[47] G. K. O. Michael, T. Connie, and A. B. J. Teoh, "A contactless biometric system using palm print and palm vein features," in *Advanced Biometric Technologies*. Rijeka, Croatia: InTech, 2011.
[48] P. Chen, B. Ding, H. Wang, R. Liang, Y. Zhang, W. Zhu, and Y. Liu, "Design of low–cost personal identification system that uses combined palm vein and palmprint biometric features," *IEEE Access*, vol. 7, pp. 15922–15931, 2019.
[49] W.-P. Choi, S.-H. Tse, K.-W. Wong, and K.-M. Lam, "Simplified Gabor wavelets for human face recognition," *Pattern Recognit.*, vol. 41, no. 3, pp. 1186–1199, Mar. 2008.
[50] A. Ross and A. Jain, "Information fusion in biometrics," *Pattern Recognit. Lett.*, vol. 24, no. 13, pp. 2115–2125, 2003.
[51] R. A. Arun and G. Rohin, "Feature level fusion of hand and face biometrics," *Proc. SPIE*, vol. 5779, pp. 196–204, Mar. 2005.
[52] K.-A. Toh and H.-L. Eng, "Between classification–error approximation and weighted least–squares learning," *IEEE Trans. Pattern Anal. Mach. Intell.*, vol. 30, no. 4, pp. 658–669, Apr. 2008.
[53] K.-A. Toh, J. Kim, and S. Lee, "Biometric scores fusion based on total error rate minimization," *Pattern Recognit.*, vol. 41, no. 3, pp. 1066–1082, Mar. 2008.
[54] X. Tan and B. Triggs, "Enhanced local texture feature sets for face recognition under difficult lighting conditions," *IEEE Trans. Image Process.*, vol. 19, no. 6, p. 1635—1650, 2010.
[55] B.-S. Oh, K. Oh, A. B. J. Teoh, Z. Lin, and K.-A. Toh, "A Gabor-based network for heterogeneous face recognition," *Neurocomputing*, vol. 261, pp. 253–265, Oct. 2017.
[56] K.-A. Toh, Q.-L. Tran, and D. Srinivasan, "Benchmarking a reduced multivariate polynomial pattern classifier," *IEEE Trans. Pattern Anal. Mach. Intell.*, vol. 26, no. 6, pp. 740–755, Jun. 2004.
[57] The Hong Kong Polytechnic University. *PolyU Multispectral Palmprint Database*. Accessed: Sep. 2017. [Online]. Available: http://www.comp.polyu.edu.hk/~biometrics/MultispectralPalmprint/MSP.html
[58] Center for Biometrics and Security Research. *Casia Multispectral Palmprint Database*. Accessed: Jan. 2018. [Online]. Available: http://biometrics.idealtest.org/
[59] The MathWorks. *MATLAB*. Accessed: Sep. 2017. [Online]. Available: http://www.mathworks.com/
[60] Z. Khan, A. Mian, and Y. Hu, "Contour code: Robust and efficient multispectral palmprint encoding for human recognition," in *Proc. IEEE Int. Conf. Comput. Vis.*, Barcelona, Spain, Nov. 2011, pp. 1935–1942.
[61] The MathWorks. *Support Vector Machine Classification*. Accessed: Jan. 2018. [Online]. Available: https://www.mathworks.com/help/stats/fitcsvm.html
[62] B. E. Boser, I. M. Guyon, and V. N. Vapnik, "A training algorithm for optimal margin classifiers," in *Proc. 5th Annu. Workshop Comput. Learn. Theory*, Pittsburgh, PA, USA, 1992, pp. 144–152.
[63] G.-B. Huang, Q.-Y. Zhu, and C.-K. Siew, "Extreme learning machine: Theory and applications," *Neurocomputing*, vol. 70, nos. 1–3, pp. 489–501, Dec. 2006.
[64] K. Pearson, "Mathematical contributions to the theory of evolution.—III. Regression, Heredity, and Panmixia," *Philos. Trans. Roy. Soc. London Ser. A*, vol. 187, pp. 253–318, Dec. 1896.

SUNGCHUL CHO received the B.S. degree in electrical and electronic engineering from Chung-Ang University, South Korea, in 2013. He is currently pursuing the Ph.D. degree in electrical and electronic engineering with Yonsei University, Seoul, South Korea. His research interests include image processing, machine learning, hand biometrics, and pattern recognition.

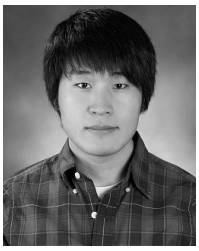

BEOM-SEOK OH received the B.S. degree in computer science from Konkuk University, South Korea, in 2008, and the M.S. degree in biometrics and the Ph.D. degree in electrical and electronic engineering from Yonsei University, South Korea, in February 2010 and August 2015, respectively. From April to November 2015, he was a Research Associate and then a Research Fellow with the School of Electrical and Electronic Engineering, Nanyang Technological University, Singapore. Since September 2019, he has been an Assistant Professor with the School of Digital Media Engineering, Tongmyong University, South Korea. His research interests include biometrics, pattern recognition, and machine learning.

KAR-ANN TOH (Senior Member, IEEE) received the Ph.D. degree from Nanyang Technological University (NTU), Singapore. He then worked for two years in the aerospace industry, prior to his postdoctoral appointments at research centers in NTU, from 1998 to 2002. He was with the Institute for Infocomm Research, Singapore, from 2002 to 2005. He is currently a Professor with the School of Electrical and Electronic Engineering, Yonsei University, South Korea. He is also a co-inventor of two U.S. patents and has made several PCT filings related to biometric applications. His research interests include biometrics, pattern classification, machine learning, optimization, and neural networks. Besides being active in publications, he has served as a member of advisory board and technical program committee for international conferences related to biometrics and artificial intelligence. He has served as an Associate Editor for the IEEE TRANSACTIONS ON INFORMATION FORENSICS AND SECURITY, from 2013 to 2016. He is also an Associate Editor of the IEEE TRANSACTIONS ON BIOMETRICS, BEHAVIOR, AND IDENTITY SCIENCE, the *Journal of The Franklin Institute*, *Pattern Recognition Letters*, and *IET Biometrics*.

ZHIPING LIN (Senior Member, IEEE) received the B.Eng. degree in control engineering from the South China Institute of Technology, Guangzhou, China, in 1982, and the Ph.D. degree in information engineering from the University of Cambridge, U.K., in 1987. He was with the University of Calgary, Canada, Shantou University, China, and DSO National Laboratories, Singapore, from 1987 to 1999. Since 1999, he has been with Nanyang Technological University (NTU), Singapore, where he is also the Program Director of the Centre for Bio Devices and Signal Analysis. His research interests include multidimensional systems and signal processing, statistical and biomedical signal processing, and machine learning. He is the coauthor of the 2007 Young Author Best Paper Award from the IEEE Signal Processing Society and the Distinguished Lecturer of the IEEE Circuits and Systems Society (CAS), from 2007 to 2008. He received several best paper awards in international conferences. He has served as the Chair of the IEEE CAS Singapore Chapter, from 2007 to 2008 and in 2019. He was an Associate Editor of the IEEE TRANSACTIONS ON CIRCUITS AND SYSTEMS II, from 2010 to 2011. He was the Editor-in-Chief of *Multidimensional Systems and Signal Processing*, from 2011 to 2015, after being on its editorial board, since 1993. He is also a Subject Editor and a Guest Editor of the *Journal of The Franklin Institute*.